WILEY | Hindawi

Research Article

Experimental and Numerical Analysis of Rock Burst Tendency and Crack Development Characteristics of Tianhu Granite

Jinzhu Hu [ID],[1,2,3] **Yajun Wang** [ID],[1,2,4] **Zimin Ma** [ID],[5] **Xingen Ma,**[6] **Xingyu Zhang,**[1,2,7] **and Guangyuan Yu**[1,2]

[1]*State Key Laboratory of Geomechanics & Deep Underground Engineering, China University of Mining and Technology, Beijing 100083, China*
[2]*School of Mechanics and Civil Engineering, China University of Mining and Technology, Beijing 100083, China*
[3]*Department of Earth Science, Florence University, Florence 50121, Italy*
[4]*Department of Geotechnical Engineering, College of Civil Engineering, Tongji University, Shanghai 200092, China*
[5]*School of Resources and Environmental Engineering, Shandong University of Technology, Zibo, Shandong 255049, China*
[6]*Huaneng Coal Technology Research CO., LTD, Beijing 100070, China*
[7]*Department of Civil, Environmental and Architectural Engineering, University of Colorado, Boulder, CO 80309, USA*

Correspondence should be addressed to Yajun Wang; yyajun1990@163.com

Rock burst is a serious nonlinear dynamic geological hazard in underground engineering construction. In this paper, a true triaxial unloading rock burst experiment and numerical simulation are carried out on Tianhu granite to investigate the rock burst tendency and crack development characteristics of surrounding rock after excavation. The experiment and numerical simulation process monitored the rock burst stress path to determine the rock burst stress. According to the evolution law of the frequency and amplitude of rock burst acoustic emission monitoring, the shape characteristics of rock burst fragments are analyzed. The rock burst numerical simulation analysis is carried out by the PFC software, and the temporal and spatial evolution law of cracks is obtained. The research results show that the laboratory experiment and numerical simulation of Tianhu granite have rock burst strengths of 163.4 MPa and 161 MPa, respectively, and the average rock burst stress ratio is 8.38, that is, the Tianhu granite has a low rock burst tendency. During the rock burst, the development of tensile cracks will produce flaky debris, and the development of shear cracks will produce lumpy debris. Rock burst will happen when the crack growth rate to be exceeded the unloading crack growth rate; therefore, it can be used as a precursor signal for the occurrence of rock burst.

1. Introduction

Rock burst is a nonlinear dynamic phenomenon in which the energy rock mass releases energy instantaneously along the excavation surface. The energy rock mass refers to the engineering rock mass with elastoplastic energy generated by the stress field including gravity, structure, and topography under certain conditions. In the mine, hydropower, transportation, and other rock engineering fields, a growing number of deep, long, and large roadways will be constructed in future. As the burial depth increases, high-strength rock bursts occur more frequently, which bring great threats to safe construction.

Therefore, rock burst has become an urgent research topic in underground engineering construction.

Experts and scholars all over the world have carried out a lot of research on rock burst from theory, experiment, field, and numerical simulation. The theoretical research of rock burst mainly focuses on rock burst prediction, using various factors that cause rock burst to evaluate the possibility and severity of rock burst. Dong used the method of Random Forest to classify whether rock burst will happen and the intensity of rock burst in the underground rock projects [1]. Adoko took a research to predict rock burst intensity based on fuzzy inference system and adaptive neuro-fuzzy

inference systems and field measurements [2]. Kornowski predicted the rock burst probability given seismic energy and factors defined by the expert method of hazard evaluation data [3]. Qiu estimated the rock burst wall-rock velocity invoked by slab flexure sources in deep tunnels [4]. Wang predicted rock burst tendency based on fuzzy matter–element model [5]. Xu established a new energy index for evaluating the tendency of rock burst and its engineering application [6]. Zhou built a long-term prediction model of rock burst in underground openings using heuristic algorithms and support vector machines [7]. He employed a modified triaxial rock testing apparatus to investigate the rock burst behavior of oriented sandstone [8]. Zhou selected four typical examples to study the mechanisms of bursts related to the structural plane and illustrate the temporal and spatial characteristics of the burst and the exposed plane [9]. Du investigated the failure behaviors of different rock types using a novel testing system coupled to true triaxial static loads and local dynamic disturbances [10]. Li provided a methodology to evaluate water-weakening effect through laboratory and numerical modelling approaches [11, 12]. Meng presented a novel mesoscale computational modeling study of SRMs with concave aggregates [13]. Meng investigated methods for predicting bursts induced by the shear failure of structural planes in the deeply buried hard rock tunnels; shear tests were performed under various normal stresses on completely occlusive granite joints that were created via tension splitting [14]. Wang created a theoretical basis for rock dynamic disaster prediction through investigating the failure mechanism of marble under FC-CPU conditions [15]. Su clarified the characteristics of remotely triggered rock burst; the development of remotely triggered rock bursts of granite rock specimens was investigated using an improved true triaxial test system [16]. Su investigated the evolutionary features of AE and sound signals, performed rock burst tests on granite rock specimens under true triaxial loading conditions using an improved rock burst testing system, and analyzed the AE and sounds during rock burst development [17]. Tao developed a model-scale NPR anchor cable according to similarity theory [18]. Wang investigated the cracking propagation and to quantify the degree of damage and the type of crack classification [19]. Yin investigated the lithology effects on their strength, macrofailure initiation (MFI), energy evolution, and failure characteristics, respectively [20]. Li described the comprehensive monitoring methods applied and results of numerical analysis applied to a typical rock burst that fortuitously occurred during the testing period to investigate the nucleation and evolution mechanism of rock bursts [21]. Lu analyzed the frequency-spectrum evolutionary rule and precursory characters in detail by experimental tests for combined coal and rock sample rock burst failure and in situ measurements in a strong rock burst coal mine [22]. Feng proposed a microseismicity-based method of rock burst warning in tunnels to warn of and reduce the risk of rock burst; the method uses real-time microseismic data and an established rock burst warning formula to provide dynamic warning of rock burst risk during excavation of a tunnel [23]. Lu investigated MS multiparameter evolutionary characteristics and EME variation of a disastrous rock burst

triggered by the intensive roof fracturing and caving combined with the static high-stress concentration by the relevant analysis techniques [24]. Ma summarized the characteristics and mechanism of rock bursts and the role of geological structures based on the great number of rock burst events recorded during construction of the headrace tunnels of Jinping II Hydropower Station. The numerical research of rock burst mainly focuses on the failure mechanism of rock burst [25]. Sharan proposed a finite element model to predict the potential occurrence of rock burst in underground openings [26]. Jiang put forward a new energy index, the Local Energy Release Rate to simulate the conditions causing rock burst in order to understand the rock burst mechanism [27]. Zhao used field data from a deep coal mine and numerical modeling to investigate the effects of gas pressure and mechanical compressive stresses on coal bursting liability in high gas content coal seams [28].

In this paper, the rock burst test and numerical analysis under true triaxial conditions are carried out on the granite 500 m underground in Tianhu Lake, Xinjiang, to reproduce the rock burst phenomenon and obtain the rock burst trigger stress conditions and study the characteristics of rock burst crack development. Under true triaxial laboratory conditions, it is possible to analyze rock burst occurrence conditions and rock burst development process in detail, explore the crack trigger mechanism of rock burst, and provide support for rock burst prediction and evaluation. The research results provide a research foundation for the prevention of rock burst during the construction of the Tianhu Underground Project.

2. Rock Burst Experiment

2.1. Experiment System. The rock burst experiment is carried out using a rock burst experimental system, which consists of a true triaxial experimental host subsystem, a hydraulic control subsystem, and a data acquisition subsystem (Figure 1). The data acquisition subsystem includes force and deformation acquisition instruments, acoustic emission monitoring, and high-speed image recording systems. The experimental system can realize the functions of three-way and six-sided independent loading and one-side sudden unloading, and the maximum loading capacity is 450 kN. Among them, the force and deformation acquisition instrument has a total of 8 channels; the sampling frequency is 1 k ~100 k resolution is 16 bit. The acoustic emission monitoring system's built-in 18-bit A/D converter and processor are suitable for low amplitude, low threshold (17 dB) settings, and 1 KHz-3 MHz frequency range. The high-speed image recording system has a resolution of 1024×1024 and a shooting speed of 1,000 fps.

2.2. Basic Situation of Samples. The granite is taken from the shallow surface of Xinjiang Tianhu. In order to understand the basic physical and mechanical properties of the selected samples (such as uniaxial compressive strength, elastic modulus, and Poisson's ratio), a small number of cylindrical (φ 50×100 mm) specimens were also prepared for uniaxial

(a)

(b)

(c)

FIGURE 1: True triaxial experimental host and hydraulic control system: (a) force and deformation acquisition system; (b) acoustic emission monitoring system; (c) high-speed image recording system.

TABLE 1: Rock uniaxial compression test results.

No.	Uniaxial compressive strength (MPa)	Young's modulus (GPa)	Poisson ratio
1#	154.9	51.88	0.29
2#	166.7	52.77	0.28
3#	166.6	46.81	0.23
Average	162.7	50.50	0.27

compression of three specimen experiment; the experimental results are shown in Table 1.

The size of the rock sample for rock burst experiments is 150 mm × 60 mm × 30 mm, totaling 3 pieces. The wave samples were subjected to shear wave and longitudinal wave tests using a wave speed tester. The test piece numbers and related physical parameters are shown in Table 2. Before the experiment, a piece of about 1 cm square was selected from the remaining debris of the more intact granite specimens, and the SEM experiment was carried out. As shown in Figure 2, when the magnification was 100x, the surface of the test piece was observed. Dense, less primary cracks, and the surface is not very flat.

2.3. Loading Path. The experiment uses the same loading and unloading method, namely, three-way six-sided loading, single-sided sudden unloading, and vertical loading. The ground stress regression formula was obtained according to the geostress test of Tianhu Lake in Xinjiang. The experiment is carried out according to the stress value $\sigma_H = 19$ MPa, $\sigma_v = 13.3$ MPa, and $\sigma_h = 12.2$ MPa obtained at a depth of about 500 m. The original rock stress state before the excavation of the diverticulum is simulated. The single-sided sudden unloading simulates the excavation process of the roadway, and the axial loading after unloading simulates the stress concentration process after excavation.

Firstly, the three-direction stress is loaded at a constant speed, and the loading rate is set to 0.1 MPa/s. When the stress in all three directions is added to the minimum principal stress σ_3, the σ_3 is kept unchanged, and the maximum principal stress σ_1 and the intermediate principal stress σ_2 are increased to a predetermined σ_2 value. Keep σ_2 and σ_3 unchanged and then increase σ_1 to the designed σ_1 stress value. After the three-way stress reaches an initial stress state corresponding to a depth of about 500 m, it is maintained for 30 minutes. Then, σ_3 is unloaded, σ_2 is kept unchanged, and σ_1 is added to simulate the stress concentration after tunnel excavation. The loading rate is 0.5 MPa/s until the rock breaks. The stress state transition process and stress path of the rock are shown in Figure 3.

3. Experiment Result Analysis

3.1. Rock Burst Failure Characteristics. In the process of rock burst experiment on Tianhu granite in Xinjiang, the failure modes of samples are local rock burst and overall rock burst, and the intensity of rock burst is obviously different (Figure 4). About 9 minutes after unloading, cracks appeared on the surface of C1 specimens, accompanied by local small particles ejection, and a small sound was emitted inside the specimens. Subsequently, flake debris ejection occurred at the bottom of the specimen, followed by a more violent flake peeling at the bottom of the specimen, which occupied about 1/3 of the area of the free surface and flew out at a higher speed after fracture, accompanied by a larger noise, a large number of debris ejection. About 3 minutes and 50 seconds after unloading of C2 specimens, internal sound occurs, fine particles pop up, followed by a large number of debris pop up quickly at the bottom of the specimens, and the sound is louder. About half of the specimens were damaged. About 6 minutes and 30 seconds after unloading of C3 specimens, there was no sign of sudden violent damage from the lower part, a large number of massive debris popped up quickly,

TABLE 2: Basic physical parameters and characteristics of granite samples.

Sample number	Density (g/cm^3)	Longitudinal wave velocity (m/s)	Shear wave velocity (m/s)	Characteristics
C-1#	2.63	4017	2910	
C-2#	2.64	3997	2831	Gray, compact, complete without cracks
C-3#	2.65	3968	3353	
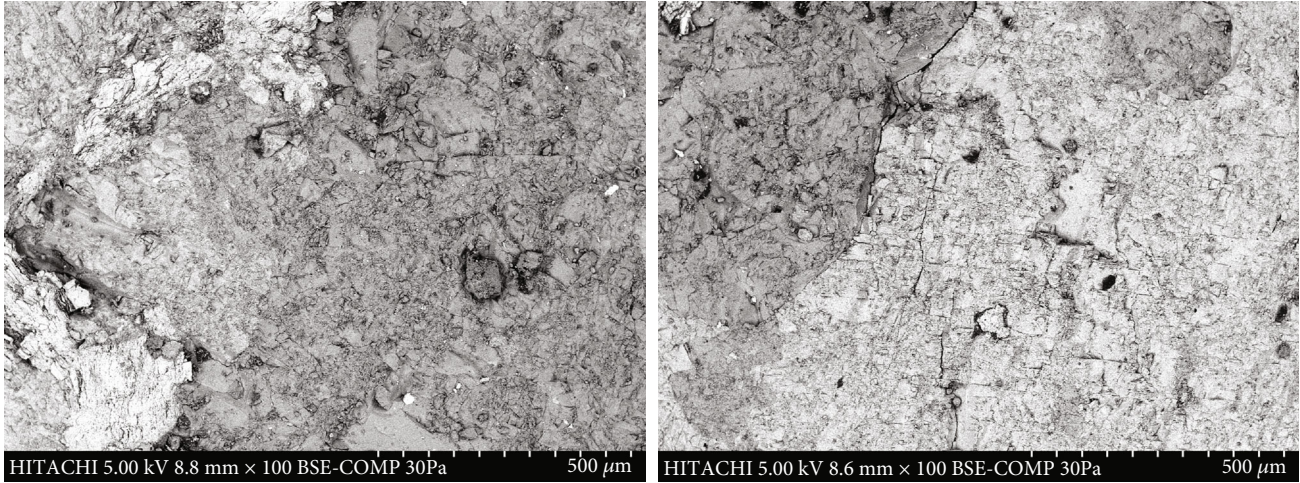
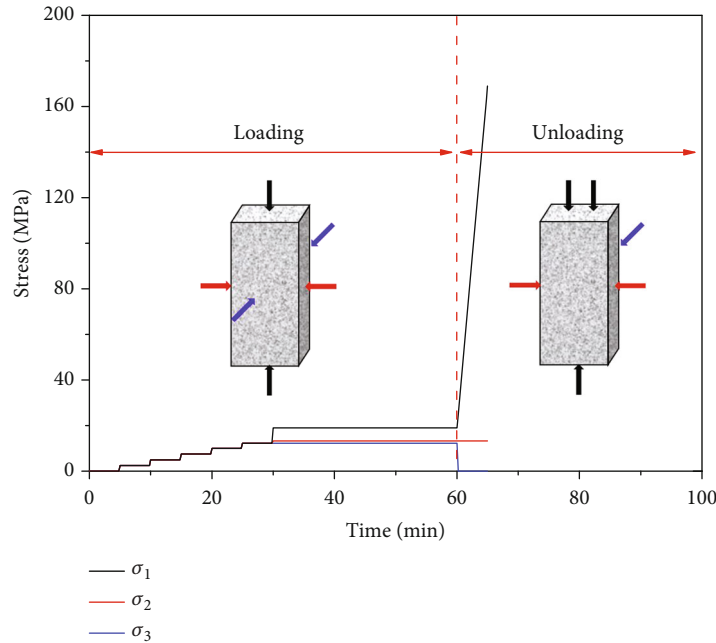FIGURE 2: Microstructure of granite before rock burst experiment.

FIGURE 3: Loading path of granite rock burst experiment.

and about half of the debris thickness of the specimens were popped out. The whole damage process lasted less than 10 seconds. During the different stage of rock burst experiment, the principal stresses are shown in Table 3. The average value of the maximum principal stress of rock burst is 163.4 MPa, and the average value of the maximum principal stress ratio of rock burst is 8.38; Tianhu granite has a low tendency to rock burst.

3.2. Acoustic Emission Characteristics. The type of rock fracture has a great relationship with the acoustic emission waveform. The acoustic emission spectrum shows that the low frequency corresponds to the tension crack in the rock, and the high frequency corresponds to the shear crack in the rock [29]. The time-frequency transformation results of the granite rock burst in Figure 5 show that the dominant frequency of acoustic emission is low frequency. The low-frequency
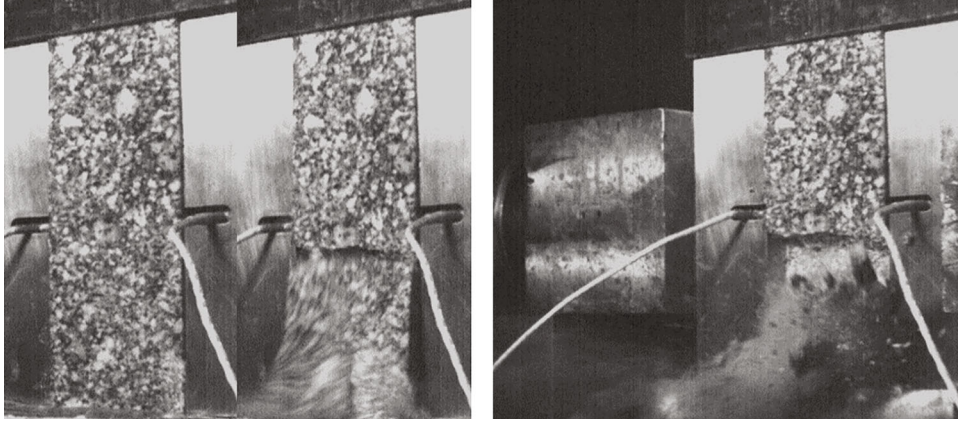
FIGURE 4: High-speed photography of failure process in rock burst experiment.

TABLE 3: Stresses in different stages during rock burst experiment.

Sample number	In situ stress (MPa) $\sigma_1/\sigma_2/\sigma_3$	Rock burst stress (MPa) $\sigma_{1r}/\sigma_{2r}/\sigma_{3r}$	Stress ratio (σ_{1r}/σ_1)
C1	19.2/13.2/12.0	159.2/13.7/0.0	8.29
C2	19.1/13.3/12.0	142.3/14.7/0.0	7.45
C3	20.1/13.0/11.9	188.7/13.4/0.0	9.39
Average	19.5/13.2/12.0	163.4/13.9/0.0	8.38

amplitude is relatively high at the beginning of the loading process, and the amplitudes of all frequency bands of acoustic emission near rock burst and rock burst destruction increase.

In Figure 5(a), the frequency band during initial loading and rock burst is mainly low frequency, and the amplitude of each frequency band during rock burst slightly increases, indicating that tension cracks are mainly damaged during initial and rock burst, and tension cracks develop rapidly during rock burst. The final rock burst fragments are in the form of flakes. In Figure 5(b), the initial loading and rock burst frequency bands are dominated by low frequency, followed by medium and high frequencies. The amplitude of the high frequency band during rock burst increases significantly, indicating that it is tensioned during rock burst. Both fractures and shear cracks developed, and there were many tension cracks, and the final rock burst fragments were flaky and massive. In Figure 5(c), the frequency band during the initial loading was low frequency, and the high frequency band and high amplitude appeared during rock burst. It shows that only tensile cracks develop in the initial stage, and shear cracks develop significantly during rock burst, and the rock burst fragments are finally large. The amplitude-frequency characteristics of acoustic emission show the development and evolution of tension cracks and shear cracks during rock burst incubation, which are macroscopically characterized by the shape of rock burst fragments.

4. Rock Burst Numerical Simulation

4.1. Model Theory. PFC (Particle Flow Code) is a general purpose, distinct-element modeling (DEM) framework; it contains ball model and contact bond model. The contact bond model provides the behavior of an infinitesimal, linear elastic, and either frictional or bonded interface that carries a point force and does not resist relative rotation. The force-displacement relationship for a bonded linear contact is that it can sustain a tensile force and precludes the possibility of slip until failure. A contact bond can be envisioned as an infinitesimally vanishing point of glue acting as a pair of elastic springs with constant stiffness kn and ks in the normal and shear directions, respectively, binding the balls together at the contact point, and allowing tensile forces to develop until a critical force failure criterion is met in the normal and/or shear direction. If bonded, the behavior is linear elastic until the strength limit is exceeded, and the bond breaks, making the interface unbonded.

Figure 6 shows a sketch of the model, introducing its main parameters. Normal and shear forces result from a combination of linear springs acting in parallel with viscous dashpots. Shear forces are always accumulated incrementally via incremental shear displacements. Normal forces, on the other hand, can be either incrementally accumulated if the normal force update mode. The contact activity status and normal force depend on the difference between the contact gap and the reference gap. Slip behavior is accommodated by imposing a Coulomb limit on the shear force using the friction coefficient. Dashpot behavior can be modified by choosing the value of the dashpot mode. The maximum normal stress σ and shear stress τ at the parallel bond periphery are updated as follows:

$$
\begin{aligned}
\sigma &= \frac{F_n}{A} + \beta \frac{F_n M_b R}{I}, \\
\tau &= \frac{F_s}{A} + \beta \frac{F_s M_t R}{J},
\end{aligned}
\tag{1}
$$

where normal force F_n and shear force F_s encompass the contributions of the linear springs and viscous dashpots, A is the contact cross-sectional area, the moment contribution factor β is a user-defined property between 0.0 and 1.0 (default is 1.0), M_b and M_t are the bending moment and twisting moment, R is the ball radius, and I and J are the
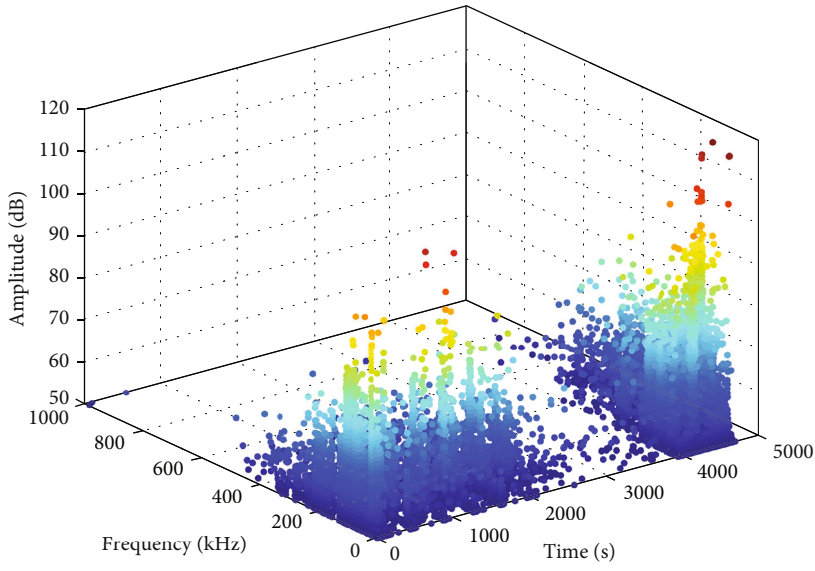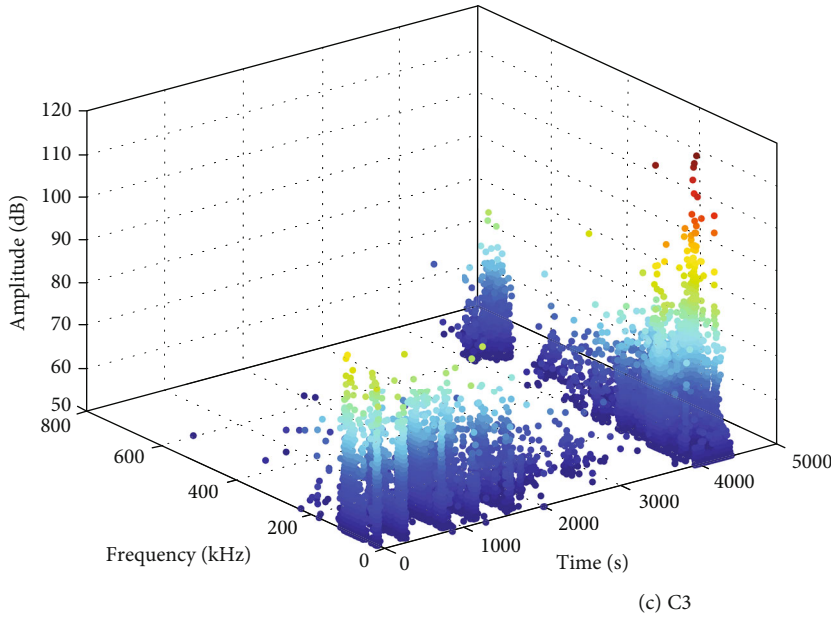
(a) C1
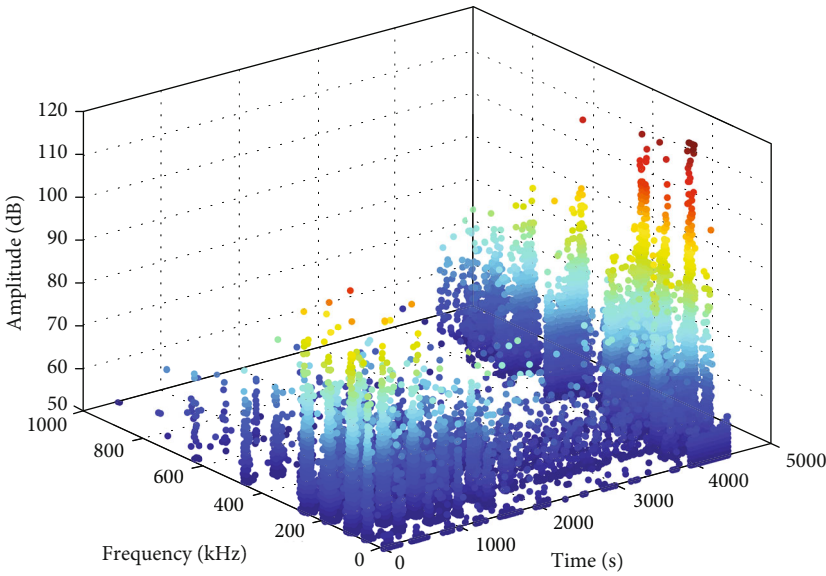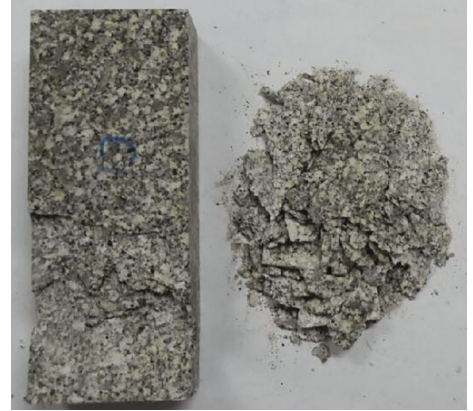
(b) C2

Figure 5: Continued.

(c) C3

FIGURE 5: Acoustic emission spectrum characteristics and fragments of rock burst in granite.

moment of inertia of an area and moment of inertia. These values are checked against the tensile and shear strengths, and the bond state is updated if the corresponding limit is exceeded. The contact model failure criterion is subjected to Mohr-coulomb criteria; if the $\sigma < \sigma_c$, the contact failed in tension; if the $\tau > \tau_c$, the contact failed in shear, as show from Figure 6.

4.2. Model Construction. The minimum particle size of the particles is 1 mm, and the particle size ratio is 1.6. The simulation adopts the flat joint bond model, which can solve the problems of low brittleness coefficient, low internal friction angle, and linear strength envelope and obtain more realistic rock mechanical properties [30]. The uniaxial compression numerical simulation calibrates the deformation modulus, stiffness ratio of the particle and the bond, and the tensile strength and cohesion of the bond. Setting the same particle and bonding parameters, after many experiments and debugging, in order to avoid the randomness of the numerical simulation results, a 10 times numerical simulation was carried out and compared with experiment (Figure 7). The results obtained are compared with the indoor experiment basically the same. The calibrated meso-parameter values are, respectively, bond deformation stiffness 3.9 GPa, bond stiffness ratio 1.8, bond tensile strength 10 MPa, bond cohesive force 56 MPa, bond internal friction angle 20, and friction coefficient 0.9.

Based on the rock burst experiment, a true triaxial unloading rock burst numerical simulation is carried out. First, the boundary of the plate sample model is established, which is composed of 6 wall elements. Then, fill the enclosed wall space with discrete spherical particles, set the density of the sphere to 3325 kg/m^3, and perform calculations on the model to achieve a uniform balance. Add contact between

particles and eliminate the force between particles in the model. The corresponding hierarchical loading and unloading programs are written through the built-in fish language to simulate the original stress state of the model and the excavation process. The loading stages are divided into 5 stages, and the three principal stresses are loaded in sequence. Displacement-controlled loading is adopted. In order to ensure the uniform stress loading speed in all directions, the moving speeds of upper wall 1, right wall 4, and front wall 5 are set to 0.005 m/s, 0.002 m/s, and 0.001 m/s, respectively. When the stress in the loading σ_1 direction reaches 2.5 MPa, the servo control of the other principal stress directions is turned off. Before loading the stress in the σ_2 direction, turn on the servo control in the σ_1 direction and load to a predetermined magnitude. In the same way, when the stress in the σ_3 direction is loaded, the servo control of the other two directions is both turned on, and the load is 2.5 MPa in all three directions. At this time, the model has completed the first level of loading, and the servo control of the three principal stress directions is turned on so that the particle velocity in the model is slowly reduced to a static equilibrium state. Then, according to the experimental design, the original stress state was loaded step by step. Perform long-term three-way servo control on the model, delete wall 5 to simulate the excavation process, and set the upper and lower wall speed to be 0.025 m/s to simulate stress concentration. Continue to load until the model breaks. The stress loading curve of rock burst numerical simulation is shown in Figure 8.

5. Result Analysis and Discussion

5.1. Failure Procedure. The PFC numerical simulation based on the indoor experiment reproduces the three periods of the indoor experiment. After staged loading, the model reaches
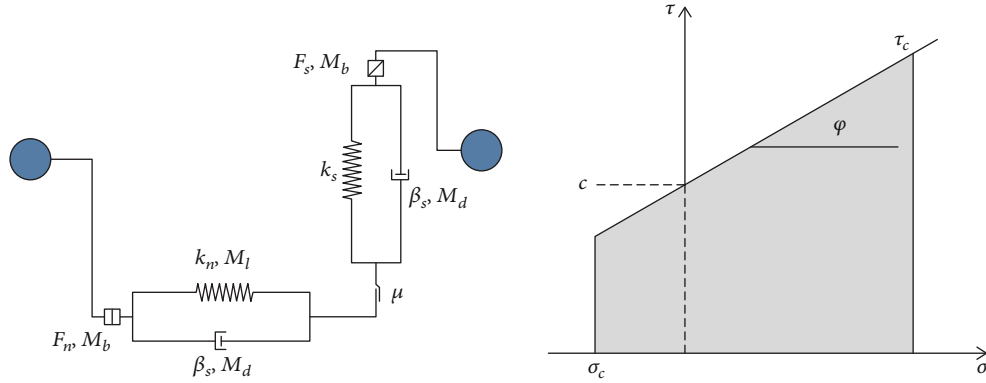
FIGURE 6: Model and failure criteria of contact bond.

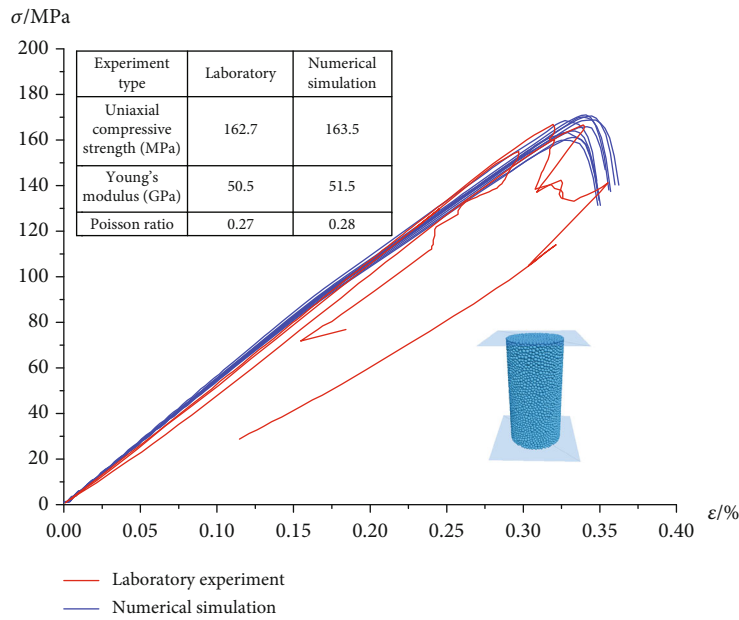| Experiment type	Laboratory	Numerical simulation
Uniaxial compressive strength (MPa)	162.7	163.5
Young's modulus (GPa)	50.5	51.5
Poisson ratio	0.27	0.28

— Laboratory experiment
— Numerical simulation

FIGURE 7: Uniaxial compression test and numerical simulation.

the original rock stress state, and the elastic strain energy continues to accumulate. Afterwards, the unloading started. After the model boundary wall 5 was deleted, the magnitude of the principal stresses all decreased. The stress path curve after unloading is shown in Figure 9. After uninstallation, the model did not change significantly. When the maximum principal stress is loaded to point A (68 MPa), the velocity field in the model increases significantly locally, and there is a phenomenon of small particles ejecting on the left side of the middle of the unloading surface. As the vertical stress reaches point B (117 MPa), the particles on the right side of the middle part of the unloading surface of the model bulge outward and separate from the main body of the model, resulting in flake peeling. The maximum principal stress is loaded to point C (126 MPa), and flaky peeling also occurs at the lower right corner of the unloading surface. The maximum principal stress reaches the peak point D (161 MPa), and damage occurs on the rear and left side of the model. The quiet period, ejection of small particles, and exfoliation in the numerical simulation are basically the same as the

indoor experiment. The size and position of the ejection of small particles and the appearance of the drum of exfoliation are similar to the indoor experiment. However, the small particle ejection and flaky exfoliation occurred in the indoor experiment at a short interval, and the numerical simulation interval was long. This is related to the degree of stress concentration. Numerical simulation can better control the stress state, while the indoor experiment is more susceptible to the interference of experimental conditions.

5.2. Temporal and Spatial Evolution Law of Cracks. In the process of numerical simulation of rock burst, cracks develop in a certain pattern (Figure 10). Loaded in stages to the original stress state, because the principal stress is much smaller than the uniaxial compressive strength, no cracks are generated in the model. When unloading, the model is in a state of nonequilibrium stress adjustment, and a small amount of cracks occur on the left and right sides of the middle of the unloading surface, mainly tensile cracks. Tensile cracks increase slowly after loading, but shear cracks remain
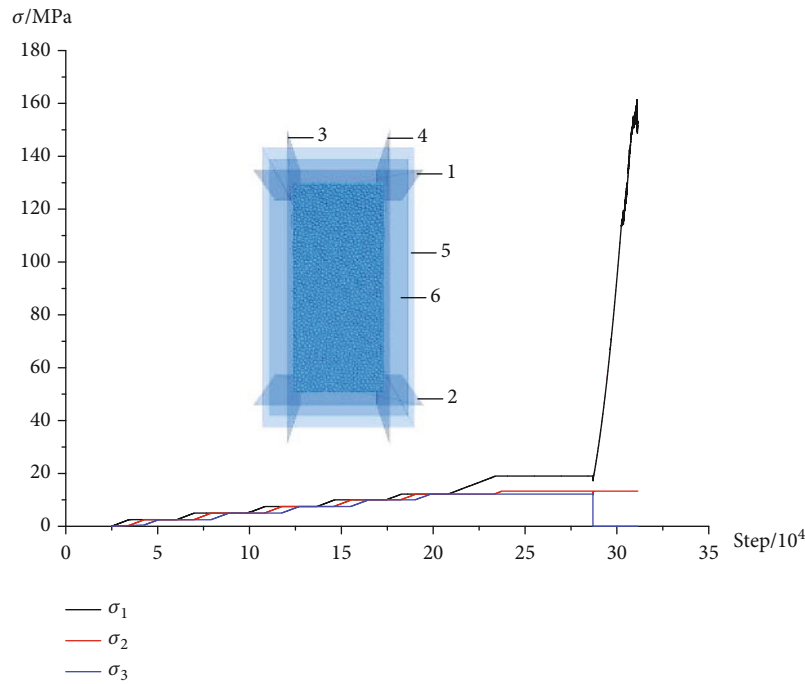
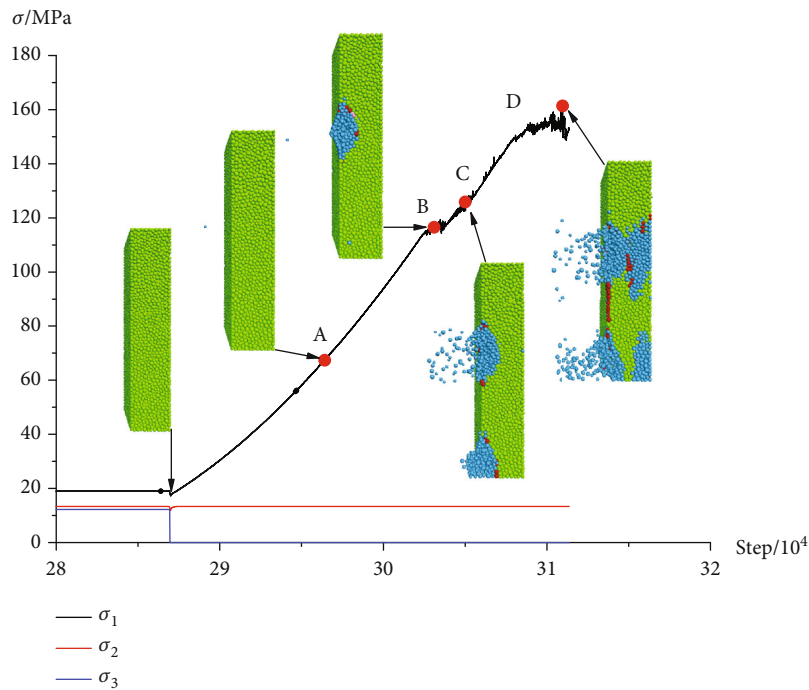FIGURE 8: Rock burst numerical model and loading path.

FIGURE 9: Rock burst failure process of the model.

unchanged. Loading from the unloading point to point A, the tensile crack growth is obvious, the shear crack growth is slow, the left crack in the middle of the unloading surface develops to the left, the shear crack develops outward, and the ejection phenomenon of small particles appears. Loading from point A to point B, both tensile and shear cracks grow rapidly, mainly concentrated on the right side of the middle of the unloading surface. After the crack penetrated, flaky

peeling occurred. Loading from point B to point C, tension and shear cracks still grow rapidly, and the cracks are mainly concentrated in the lower right corner of the unloading surface, accompanied by flaky peeling. Loading from point C to point D, the cracks grow sharply, mainly from the middle surface of the model to the inside. After the peak strength, cracks continued to grow sharply, and other parts of the model were also damaged. The crack development in the
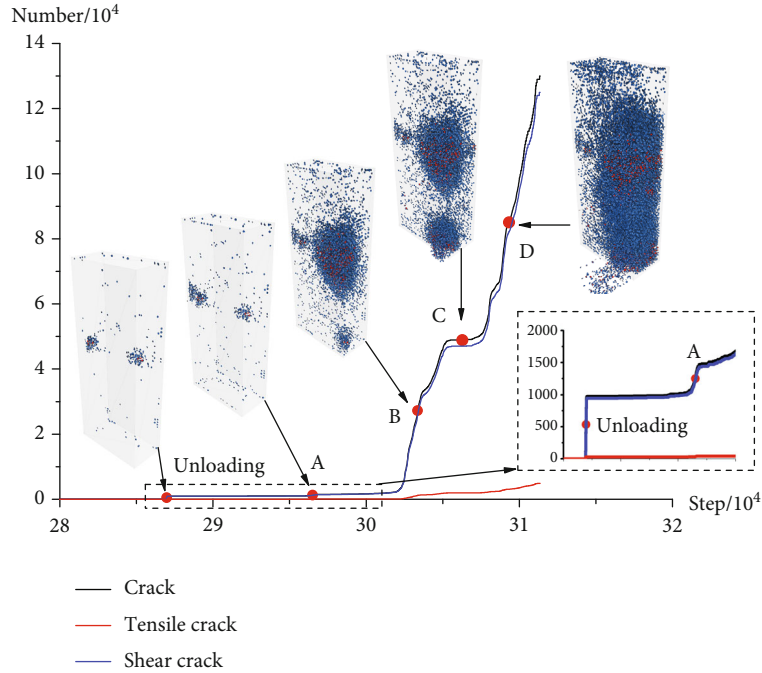
FIGURE 10: Crack time space evolution process.

model shows the characteristics of the surface and the inside in space [23]. The fresh cracks generated after unloading has a guiding effect on the location of the rock burst. The crack development in the model mainly experienced three stages of small instantaneous development-slow development-rapid development. These three stages represent excavation-rock burst incubation-rock burst in actual engineering.

5.3. Crack Growth Rate. According to the crack growth rate curve (Figure 11), the failure of the model corresponds to the growth of shear cracks, and the more severe the model is damaged, the faster the growth rate of shear cracks. When large failure phenomena such as flaky peeling occur, both the tensile and shear crack development rate suddenly increase and then rapidly decrease, and the amplitude is greater than the crack development rate during unloading. There are major differences between rock bursts that occur during TBM tunneling and D&B tunneling including the intensity and frequency of rock bursts. This difference may be due to the degree of excavation damage; D&B tunneling has a greater degree of excavation damage, so the energy required for rock burst is higher, and the frequency of rock burst is lower but intense than TBM tunneling. Therefore, the rock burst will happen when the crack growth rate to be exceeded the unloading crack growth rate; it can be used as a precursor signal for the occurrence of rock burst.
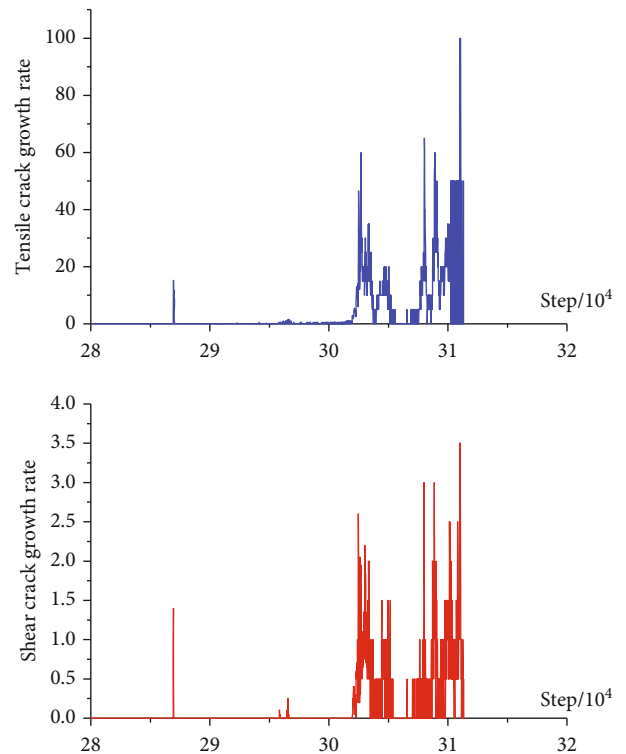
6. Conclusion

According to the laboratory experiment of Xinjiang granite true triaxial unloading rock burst and using PFC to simulate true triaxial unloading rock burst, the following conclusions are obtained:

FIGURE 11: Crack growth rate curve.

(1) The laboratory experiment and numerical simulation rock burst stress values in the granite at a buried depth of 500 m in Tianhu, Xinjiang, are 163.4 and 161 MPa, respectively, which are about 8.38 times of the maximum in situ stress. The surrounding rock

has a low tendency of rock burst when excavating a roadway at this depth

(2) The development characteristics of rock burst cracks based on acoustic emission spectrum analysis are related to the shape of debris. Tension cracks with high-amplitude and low-frequency characteristics before rock burst lead to the generation of a large number of flaky debris, while shear cracks with high-amplitude and high-frequency characteristics cause a large number of the generation of lumpy debris

(3) The temporal and spatial characteristics of rock burst cracks have certain rules based on PFC numerical simulation. Spatially, a large number of tension cracks concentrated on the unloading surface were generated during unloading. Before the rock burst, the cracks gradually developed and penetrated into the interior, and the tension cracks were far more than the shear cracks. The rock burst occurred at random locations. The occurrence of rock burst is closely related to the rate of crack development. When unloading, the rate of crack development increases suddenly. If the rate of crack development is lower than this value, only small particles will be ejected while a rock burst will occur if it exceeds this value

Data Availability

All data, model, and code generated or used during the study appear in the submitted article are available from the corresponding author upon request.

Conflicts of Interest

The authors declare that there is no conflict of interest regarding the publication of this paper.

Acknowledgments

References

[1] L. J. Dong, X. B. Li, and K. Peng, "Prediction of rockburst classification using Random Forest," *Transactions of Nonferrous Metals Society of China*, vol. 23, no. 2, pp. 472–477, 2013.

[2] A. C. Adoko, C. Gokceoglu, L. Wu, and Q. J. Zuo, "Knowledge-based and data-driven fuzzy modeling for rockburst prediction," *International Journal of Rock Mechanics and Mining Sciences*, vol. 61, pp. 86–95, 2013.

[3] J. Kornowski and J. Kurzeja, "Prediction of rockburst probability given seismic energy and factors defined by the expert method of hazard evaluation (MRG)," *Acta Geophysica*, vol. 60, no. 2, pp. 472–486, 2012.

[4] S. Qiu, X. Feng, C. Zhang, and T. Xiang, "Estimation of rockburst wall-rock velocity invoked by slab flexure sources in deep tunnels," *Canadian Geotechnical Journal*, vol. 51, no. 5, pp. 520–539, 2014.

[5] C. Wang, A. Wu, H. Lu, T. Bao, and X. Liu, "Predicting rockburst tendency based on fuzzy matter-element model," *International Journal of Rock Mechanics and Mining Sciences*, vol. 75, pp. 224–232, 2015.

[6] J. Xu, J. Jiang, N. Xu, Q. Liu, and Y. Gao, "A new energy index for evaluating the tendency of rockburst and its engineering application," *Engineering Geology*, vol. 230, pp. 46–54, 2017.

[7] J. Zhou, X. Li, and X. Shi, "Long-term prediction model of rockburst in underground openings using heuristic algorithms and support vector machines," *Safety Science*, vol. 50, no. 4, pp. 629–644, 2012.

[8] M. C. He, W. Nie, Z. Y. Zhao, and W. Guo, "Experimental investigation of bedding plane orientation on the rockburst behavior of sandstone," *Rock Mechanics and Rock Engineering*, vol. 45, no. 3, pp. 311–326, 2012.

[9] H. Zhou, F. Z. Meng, C. Q. Zhang, D. W. Hu, F. J. Yang, and J. J. Lu, "Analysis of rockburst mechanisms induced by structural planes in deep tunnels," *Bulletin of Engineering Geology and the Environment*, vol. 74, pp. 1435–1451, 2014.

[10] K. Du, M. Tao, X. B. Li, and J. Zhou, "Experimental study of slabbing and rockburst induced by true-triaxial unloading and local dynamic disturbance," *Rock Mechanics and Rock Engineering*, vol. 49, no. 9, pp. 3437–3453, 2016.

[11] Z. Li, S. Liu, W. Ren, J. Fang, Q. Zhu, and Z. Dun, "Multiscale laboratory study and numerical analysis of water-weakening effect on shale," *Advances in Materials Science and Engineering*, vol. 2020, Article ID 5263431, 14 pages, 2020.

[12] Z. Li, H. Liu, Z. Dun, L. Ren, and J. Fang, "Grouting effect on rock fracture using shear and seepage assessment," *Construction and Building Materials*, vol. 242, article 118131, 2020.

[13] Q. Meng, H. Wang, M. Cai, W. Xu, X. Zhuang, and T. Rabczuk, "Three-dimensional mesoscale computational modeling of soil-rock mixtures with concave particles," *Engineering Geology*, vol. 277, p. 105802, 2020.

[14] F. Meng, H. Zhou, Z. Wang et al., "Experimental study on the prediction of rockburst hazards induced by dynamic structural plane shearing in deeply buried hard rock tunnels," *International Journal of Rock Mechanics and Mining Sciences*, vol. 86, pp. 210–223, 2016.

[15] Y. Wang, W. K. Feng, R. L. Hu, and C. H. Li, "Fracture evolution and energy characteristics during marble failure under triaxial fatigue cyclic and confining pressure unloading (FC-CPU) conditions," *Rock Mechanics and Rock Engineering*, vol. 11, 2020.

[16] G. Su, X. Feng, J. Wang, J. Jiang, and L. Hu, "Experimental study of remotely triggered rockburst induced by a tunnel axial dynamic disturbance under true-triaxial conditions," *Rock Mechanics and Rock Engineering*, vol. 50, no. 8, pp. 2207–2226, 2017.

[17] G. S. Su, Y. J. Shi, X. T. Feng, J. Q. Jiang, J. Zhang, and Q. Jiang, "True-triaxial experimental study of the evolutionary features of the acoustic emissions and sounds of rockburst processes," *Rock Mechanics and Rock Engineering*, vol. 51, pp. 375–389, 2018.

[18] Z. Tao, C. Zhu, M. He, and M. Karakus, "A physical modeling-based study on the control mechanisms of Negative Poisson's ratio anchor cable on the stratified toppling deformation of anti- inclined slopes," *International Journal of Rock Mechanics and Mining Sciences*, vol. 138, article 104632, 2021.

[19] Y. Wang, B. Zhang, S. H. Gao, and C. H. Li, "Investigation on the effect of freeze-thaw on fracture mode classification in marble subjected to multi-level cyclic loads," *Theoretical and Applied Fracture Mechanics*, vol. 111, article 102847, 2021.

[20] D. Yin, S. Chen, Y. Ge, and R. Liu, "Mechanical properties of rock-coal bi-material samples with different lithologies under uniaxial loading," *Journal of Materials Research and Technology*, vol. 10, pp. 322–338, 2021.

[21] S. J. Li, X. T. Feng, Z. H. Li, B. R. Chen, C. Q. Zhang, and H. Zhou, "In situ monitoring of rockburst nucleation and evolution in the deeply buried tunnels of Jinping II hydropower station," *Engineering Geology*, vol. 137-138, pp. 85–96, 2012.

[22] C. P. Lu, L. M. Dou, N. Zhang et al., "Microseismic frequency-spectrum evolutionary rule of rockburst triggered by roof fall," *International Journal of Rock Mechanics and Mining Sciences*, vol. 64, pp. 6–16, 2013.

[23] G. L. Feng, X. T. Feng, B. R. Chen, Y. X. Xiao, and Y. Yu, "A microseismic method for dynamic warning of rockburst development processes in tunnels," *Rock Mechanics and Rock Engineering*, vol. 48, pp. 2061–2076, 2015.

[24] C. P. Lu, G. J. Liu, Y. Liu, N. Zhang, J. H. Xue, and L. Zhang, "Microseismic multi-parameter characteristics of rockburst hazard induced by hard roof fall and high stress concentration," *International Journal of Rock Mechanics and Mining Sciences*, vol. 76, pp. 18–32, 2015.

[25] T. H. Ma, C. A. Tang, L. X. Tang, W. D. Zhang, and L. Wang, "Rockburst characteristics and microseismic monitoring of deep-buried tunnels for Jinping II Hydropower Station," *Tunnelling and Underground Space Technology*, vol. 49, pp. 345–368, 2015.

[26] S. K. Sharan, "A finite element perturbation method for the prediction of rockburst," *Computers & Structures*, vol. 85, no. 17-18, pp. 1304–1309, 2007.

[27] Q. Jiang, X. T. Feng, T. B. Xiang, and G. S. Su, "Rockburst characteristics and numerical simulation based on a new energy index: a case study of a tunnel at 2,500 m depth," *Bulletin of Engineering Geology and the Environment*, vol. 69, no. 3, pp. 381–388, 2010.

[28] H. Zhao and R. Kaunda, "Numerical assessment of the influences of gas pressure on coal burst liability," *Energies*, vol. 11, no. 2, p. 260, 2018.

[29] S. H. Chang and C. I. Lee, "Estimation of cracking and damage mechanisms in rock under triaxial compression by moment tensor analysis of acoustic emission," *International Journal of Rock Mechanics and Mining Sciences*, vol. 41, no. 7, pp. 1069–1086, 2004.

[30] A. Y. Ma, F. Q. Wu, P. Sha, F. Zhao, and B. C. Sheng, "Progressive failure of Jinping marble in true triaxial rockburst test," *Chinese Journal of Rock Mechanics and Engineering*, vol. 10, pp. 2868–2874, 2014.